

Minute-cadence observations on Galactic plane with Wide Field Survey Telescope (WFST): Overview, methodology and early results

JIE LIN,^{1,2} TINGUI WANG,^{1,2,3} MINXUAN CAI,^{1,2} ZHEN WAN,^{1,2} XU ZHI LI,^{1,2,4} LULU FAN,^{1,2,3} QINGFENG ZHU,^{1,2} JI-AN JIANG,^{1,2} NING JIANG,^{1,2} XU KONG,^{1,2,3} ZHEYU LIN,^{1,2} JIAZHENG ZHU,^{1,2} ZHENGYAN LIU,^{1,2} JIE GAO,⁵ BIN LI,⁶ FENG LI,⁵ MING LIANG,⁷ HAO LIU,⁵ WEI LIU,⁶ WENTAO LUO,³ JINLONG TANG,⁸ HAIREN WANG,⁶ JIAN WANG,^{5,3} YONGQUAN XUE,^{1,2} DAZHI YAO,⁶ HONGFEI ZHANG,⁵ XIAOLING ZHANG,⁶ WEN ZHAO,^{1,2} AND XIANZHONG ZHENG⁶

¹*Department of Astronomy, University of Science and Technology of China, Hefei 230026, People's Republic of China**

²*School of Astronomy and Space Science, University of Science and Technology of China, Hefei 230026, People's Republic of China*

³*Deep Space Exploration Laboratory, Hefei 230088, People's Republic of China*

⁴*Institute of Astronomy and Astrophysics, Anqing Normal University, Anqing, Anhui, 246133, People's Republic of China*

⁵*State Key Laboratory of Particle Detection and Electronics, University of Science and Technology of China, Hefei 230026, People's Republic of China*

⁶*Purple Mountain Observatory, Chinese Academy of Sciences, Nanjing 210023, People's Republic of China*

⁷*National Optical Astronomy Observatory (NSF's National Optical-Infrared Astronomy Research Laboratory), 950 N Cherry Ave., Tucson, AZ 85726, USA*

⁸*Institute of Optics and Electronics, Chinese Academy of Sciences, Chengdu 610209, People's Republic of China*

ABSTRACT

As the time-domain survey telescope of the highest survey power in the northern hemisphere currently, Wide Field Survey Telescope (WFST) is scheduled to hourly/daily/semi-weekly scan northern sky up to ~ 23 mag in four optical (*ugri*) bands. Unlike the observation cadences in the forthcoming regular survey missions, WFST performed “staring” observations toward Galactic plane in a cadence of ≈ 1 minute for a total on-source time of about 13 hours, during the commissioning and pilot observation phases. Such an observation cadence is well applied in producing densely sampling light curves and hunting for stars exhibiting fast stellar variabilities. Here we introduce the primary methodologies in detecting variability, periodicity, and stellar flares among a half million sources from the minute-cadence observations, and present the WFST *g*-/*r*-band light curves generated from periodic variable stars and flaring stars. Benefit from high photometric precisions and deep detection limits of WFST, the observations have captured several rare variable stars, such as a variable hot white dwarf (WD) and an ellipsoidal WD binary candidate. By surveying the almost unexplored parameter spaces for variables, WFST will lead to new opportunities in discovering unique variable stars in the northern sky.

Keywords: surveys – stars: flare – (stars:) binaries (including multiple): close – stars: oscillations (including pulsations)

1. INTRODUCTION

Over the last decade, numerous frontier topics on fast stellar variabilities with time scales of minutes to hours have emerged. They involve ultracompact binaries (UCBs, Burdge et al. 2019, 2020; Lin et al. 2024), blue large-amplitude pulsators (BLAPs, Pietrukowicz et al. 2017; Lin et al. 2023a), rapidly rotating magnetic white dwarfs (WDs; Caiazzo et al. 2021; Williams et al. 2022), transitional cataclysmic variables (CVs; Burdge

et al. 2022a), black widows (Burdge et al. 2022b), and fast flaring stars (Günther et al. 2020; Aizawa et al. 2022; Howard & MacGregor 2022; Liu et al. 2023). The fast stellar variabilities imply extraordinary physical conditions in pulsation, rotation, orbital motion, or magnetic field for these variable stars, and thus provide crucial windows to study the stellar physics under extreme conditions.

UCBs are a class of binaries with orbital periods shorter than ~ 70 min. Due to their compact orbits, UCBs avoid to harbor a main-sequence component star (Rappaport et al. 1982), and is thus composed of neu-

* linjie2019@ustc.edu.cn

Table 1. Basic information for WFST minute-cadence observations.

Observation	Target	Field direction	N_{epoch}	Filter	Exposure (s)	Start Time (UTC)	End Time (UTC)
GP-20230918*	J0526+5934	05 : 26 : 10.43 + 59 : 34 : 45.1	165	<i>g</i>	20	2023-09-18 18:20:05	2023-09-18 21:20:29
GP-20231116	J0526+5934	05 : 26 : 10.43 + 59 : 34 : 45.1	254	<i>g</i>	20	2023-11-16 20:03:47	2023-11-16 23:22:38
GP-20240206 ⁺	Platais 3	04 : 39 : 54.24 + 71 : 16 : 48.0	130	<i>g</i>	20	2024-02-06 12:06:36	2024-02-06 15:54:46
GP-20240209	Platais 3	04 : 39 : 54.24 + 71 : 16 : 48.0	258	<i>g</i>	20	2024-02-09 12:10:52	2024-02-09 15:43:02
GP-20240509	Collinder 350	17 : 48 : 04.32 + 01 : 31 : 30.0	176	<i>r</i>	30	2024-05-09 17:57:13	2024-05-09 20:45:26

NOTE—*Because the operation control system (OCS, [Zhu et al. 2024](#)) started to work since 2023 October 30th, the observation GP-20230918 was executed manually.

⁺Due to technical tests, GP-20240206 was occasionally interrupted for 73.3 minutes.

tron star (NS; [Lin & Yu 2018](#); [Wang et al. 2021](#)), WD ([Burdge et al. 2020](#); [Ren et al. 2023](#)), or hot subdwarf ([Finch et al. 2022](#); [Lin et al. 2024](#)). A part of UCBs are predicted to generate strong gravitational wave (GW) radiation in millihertz (mHz) passband and are thus detectable from space-borne GW detectors, e.g. Tianqin ([Huang et al. 2020](#)) and Laser Interferometer Space Antenna (LISA, [Amaro-Seoane et al. 2017](#)). Since most UCBs are unresolved in the GW detectors and their GW signals are superposed incoherently, millions of UCBs in our Galaxy will produce a stochastic foreground signal (i.e. confusion noise, [Hils et al. 1990](#); [Ruiter et al. 2010](#)). Fortunately, beyond the confusion noise, space-borne GW detectors will be able to resolve tens of thousands of the UCBs. Nowadays, time-domain survey telescopes are capable of searching for these “verification” UCBs individually from electromagnetic observations in advance, and thus guarantee the operations of the GW detectors.

BLAPs represent a rare class of short-period, large-amplitude hot pulsating stars ([Pietrukowicz et al. 2017](#)). Since the BLAPs were first discovered with the Optical Gravitational Lensing Experiment (OGLE), dozens of BLAPs (or candidates) have been identified successively ([Kupfer et al. 2019](#); [Lin et al. 2022](#); [McWhirter & Lam 2022](#); [Pigulski et al. 2022](#); [Borowicz et al. 2023a,b](#); [Chang et al. 2024](#)). So far, three candidate stellar models have been proposed for understanding the physical origin of BLAPs: helium-core pre-white dwarfs (pre-WD; [Córscico et al. 2019](#); [Byrne & Jeffery 2020](#); [Byrne et al. 2021](#)), core helium-burning (CHeB) subdwarfs ([Byrne & Jeffery 2018](#); [Wu & Li 2018](#); [Meng et al. 2020](#)), and shell helium-burning (SHeB) subdwarfs ([Xiong et al. 2022](#); [Lin et al. 2023a](#)). However, due to deficient and in-homogeneous samples, the physical origin of BLAPs is still controversial. As introduced by [Lin et al. \(2023a\)](#), BLAPs may have diverse origins, and the rates of period changes play a crucial role in diagnosing their natures. With the operations of large-aperture survey missions, the growing BLAP samples and their

monitoring data will essentially improve the understanding of these mysterious hot pulsating stars.

Stellar flares are dramatically explosive phenomena triggered by impulsive magnetic reconnection in the corona, potentially accompanied by coronal mass ejections (CMEs, [Argiroffi et al. 2019](#)), relativistic electron beams ([Reid et al. 2014](#)), and chromospheric evaporation ([Güdel et al. 2002](#)). However, since the typical timescales of optical flares are from minutes to hours, the daily-/hour-cadence survey missions fail to reproduce temporal flare structures, leading to incorrect estimations for the amplitudes, durations, and energies of flares ([Yang et al. 2018](#)). Hence, the minute-cadence observations, especially executed by large-aperture, wide-field instruments, will provide rare opportunities to glimpse the flare profiles from those dark dwarf stars. In the future, the ultrashort observation cadence (≈ 0.3 second) of Tianyu project ([Feng et al. 2024a](#)) even allows us trace the rapid rise phases of flares and thus helps understand the detail process of magnetic energy release in dwarf stars.

Aiming at hunting the fast stellar variabilities in Galaxy, a few wide-field instruments started performing high-cadence survey missions, e.g. Zwicky Transient Facility (ZTF, [Masci et al. 2019](#); [Bellm et al. 2019](#)) high-cadence Galactic plane survey ([Kupfer et al. 2021](#)), OmegaWhite ([Macfarlane et al. 2015](#); [Toma et al. 2016](#)), and Tsinghua University–Ma Huateng Telescopes for Survey (TMTS, [Zhang et al. 2020](#); [Lin et al. 2022](#); [Guo et al. 2024](#)). Benefit from densely sampling photometry, these missions can well capture the fast light variations from diverse variable stars. In order to explore the fast stellar variabilities in deeper fields, we conducted a minute-cadence survey on Galactic plane with Wide Field Survey Telescope (WFST, [Lou et al. 2016](#); [Wang et al. 2023a](#)). Thanks to its 2.5-meter primary mirror, 6.5-square-degree field of view (FoV), and 0.765-gigapixel mosaic CCD camera ([Zhang et al. 2024](#); [Geng et al. 2024](#); [Feng et al. 2024b](#)), it is highly efficient for WFST to capture variable stars with brightness up to ≈ 23 mag (in *g*, *r* bands, [Lei et al. 2023](#)). In this

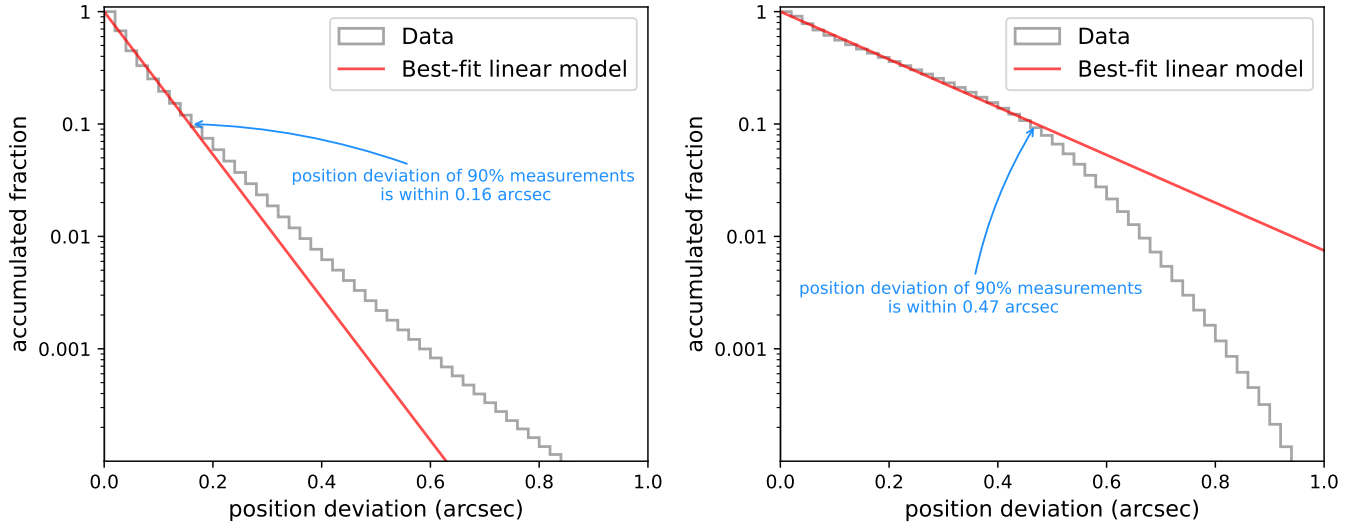


Figure 1. Accumulated fractions for the position deviations given from the minute-cadence observations on February 9th, 2024. *Left:* Position deviations anchored at average coordinates of position measurements. *Right:* Position deviations anchored at the coordinates from the first detections of sources. The bin width is 0.02 arcsec, and the red lines represent best-fit linear models for the bins with an accumulated fraction $> 10\%$.

paper, we present an overview for the WFST minute-cadence Galactic plane survey executed in its commissioning observation phase (2023.09 – 2024.02) and pilot survey phase (2024.03 – 2024.06).

2. OBSERVATIONS

Since the commissioning of WFST on 2023 September, we have performed minute-cadence observations on Galactic plane for 5 times, with a total duration of about 13 hours. As shown in Table 1, these observations were executed uninterruptedly for 3–4 hours, except for the observation GP-20240206 being occasionally interrupted for 73.3 minutes¹. With a dead time (caused by overhead) of about 30 seconds, the observation cadences are ≈ 50 s and ≈ 60 s for 20s-exposure and 30s-exposure campaigns, respectively. Notice that, since GP-20230918 was executed manually, the cadence in this observation is non-uniform in an average cadence of about 61 seconds. All these observations covered 3 non-overlapping fields (i.e. J0526+5934, Platais 3 and Collinder 350), corresponding to a total unrepeated area of ≈ 20 deg². Among them, J0526+5934 and Platais 3 were visited twice for capturing general periodic variable stars², while Collinder 350 was simultaneously observed with both WFST and Australian Square Kilometre Array

Pathfinder (ASKAP; Murphy et al. 2013, 2021; Wang et al. 2023b).

The WFST raw data were primarily dealt with the modified version of the LSST pipeline (Jurić et al. 2017), which is developed for the general purpose of the photometric data reduction. For the single frame processing, the pipeline contains several basic steps. First, the instrumental signatures were removed with the corresponding calibration exposures, including bias, (sky) flats, fringe and cross-talk. The instrumental-signatures-removed images were then labeled pixel-by-pixel with blending, saturation, cosmic ray contamination etc, indicating which part of the images should be ignored or carefully considered in the further analysis. The background was estimated as the median value of each 512×512 pixel sub-region on the image. A 2-dimensional 6th-order Chebyshev polynomial was applied in both the X and the Y directions to derive a smooth distribution of the background, and finally produced a background image and a background-subtracted science image. Sources were then detected within the background-subtracted science images, and images’ point-spread-functions (PSF) were estimated with a selected sub-sample of the sources. The flux of the sources were measured in both diverse apertures (4.5–70 pixels) and in PSF modelling, which were finally calibrated with external references—the astrometric parameters are calibrated to the Gaia DR3 (Gaia Collaboration et al. 2016, 2022) and the g -/ r -band photometric parameters are calibrated to PanStarr DR2 (Chambers et al. 2016; Magnier et al. 2020; Flewelling et al. 2020). Throughout this work, all photometric fluxes were cali-

¹ Because the interruption time is far shorter than a day, we still refer to GP-20240206 as an uninterrupted observation throughout this paper.

² In this work, we refer to the variable stars with period longer than those typical short-period variable stars as general periodic variable stars, e.g. EW eclipsing binaries and RR Lyrae stars.

brated to AB magnitudes, and the times corresponding to exposure midpoints were converted into barycentric modified Julian dates with barycentric dynamical time (BMJD_{TDB}).

All WFST photometric measurements labeled with blending, saturation, cosmic ray, and closing to the image edge were discarded throughout this work. By cross-matching the photometric measurements within a radius of 1 arcsec, we extracted light curves for all sources within the fields. For checking whether the 1-arcsec radius is large enough to bind all photometric measurements from same sources, we additionally investigate astrometric deviations for all WFST sources with epochs more than 20. The deviations were given by the angular separations between each position measurements and anchored coordinates, i.e. the average coordinates of sources here. As shown in the left panel of Fig. 1, the accumulated fractions suggest that, the astrometric precision of WFST is better than 0.16 arcsec for 90% measurements in these early observations. However, since we tend to take the position measurements from first detections as the coordinates of sources, rather than the average ones, a larger radius should be adopted in cross-matching (see the right panel of Fig. 1). Here the 1-arcsec radius ensures an $\approx 0.01\%$ possibility at most that a measurement from a source cannot match its first detection, which effectively prevents splitting a source into multiple sources.

3. METHODS

In order to select diverse variables from millions of WFST light curves, we applied three different algorithms in the light-curve analysis (LCA, Sokolovsky et al. 2017), namely von Neumann ratio η , Osten’s method (Osten et al. 2012), and Lomb–Scargle periodogram (LSP, Lomb 1976; Scargle 1982). Since Lin et al. (2022) has detailed how these algorithms worked on the uninterruptedly light curves obtained from minute-cadence survey observations, here we introduce only the basic principles for these algorithms and their performances for WFST observation data. Furthermore, we also cross-match the WFST sources with Gaia DR3 catalog (Gaia Collaboration et al. 2016, 2022) for locating them in color-magnitude diagram (CMD), which plays a crucial role in preliminary identifications of variable stars.

3.1. Variability detection

In order to test the variability detection in the observation data, we extracted light curves (with ≥ 20 epochs) from g -band observation GP-20240209 and r -band observation GP-20240509. Among them, GP-20240209

contributed 119,199 uninterrupted light curves, while GP-20240509 provided 262,628 ones. The statistical characteristics for these light curves are presented in Fig. 2. In the g -band observations, the WFST light curves are distributed dominantly from 12.9 to 22.5 mag, and the number of light curves increases along with the median magnitude and peaks around 22 mag. Due to low altitude angle (from 35° to 50°) and thus large atmospheric extinction over the observation GP-20240509, the median magnitudes of r -band light curves here range from 12.2 to 20.6 mag. **Notice that, because of the fact that the minute-cadence observations were executed within a single night and covered only a sky plate, the magnitude distributions here should not be used to demonstrate the limiting magnitudes for WFST.**

Similar to the standard deviation (StD), robust StD is a variability index quantifying the scatter of brightness measurements based on 25 percentile of the measurements above/below the median. Because only inner 50 percentile of the measurements are used to derive the StD (see also Ofek et al. 2020), robust StD is immune from outliers or occasional real variations (e.g. fast flares). As shown in the middle panels of Fig. 2, the robust StD raises from 0.008 mag to ~ 0.2 mag with the darkening of sources, while the variation trend represents the photometric uncertainties at various magnitudes. The light curves that present significantly larger scatters than the expected uncertainties, are likely generated from variable sources. By fitting the 10σ excesses at various magnitudes with 5th-order polynomial models, 462 candidate variable sources and 634 ones were selected from GP-20240209 and from GP-20240509, respectively, implying about 3 candidate variables among per 1,000 observed sources. However, due to blending, saturation, stray lights, and varying atmospheric extinction with the altitude, the candidate variable sources inevitably include a large proportion of non-astrophysically variable sources³. As Kupfer et al. (2021) introduces, about 60%-85% of the candidate variable sources present spurious variations from the ZTF high-cadence observations, especially in those crowded fields; Lin et al. (2022) also revealed a false positive rate⁴ of 67% from their 10σ -excess variable candidates in the first-year minute-cadence observations of TMTS. By visually checking the WFST light curves from all candidate variable sources, we found that the false positive

³ The sources with light variations that are not caused by real astrophysical variability.

⁴ The ratio of the non-astrophysically variable sources to the all candidate variable sources here.

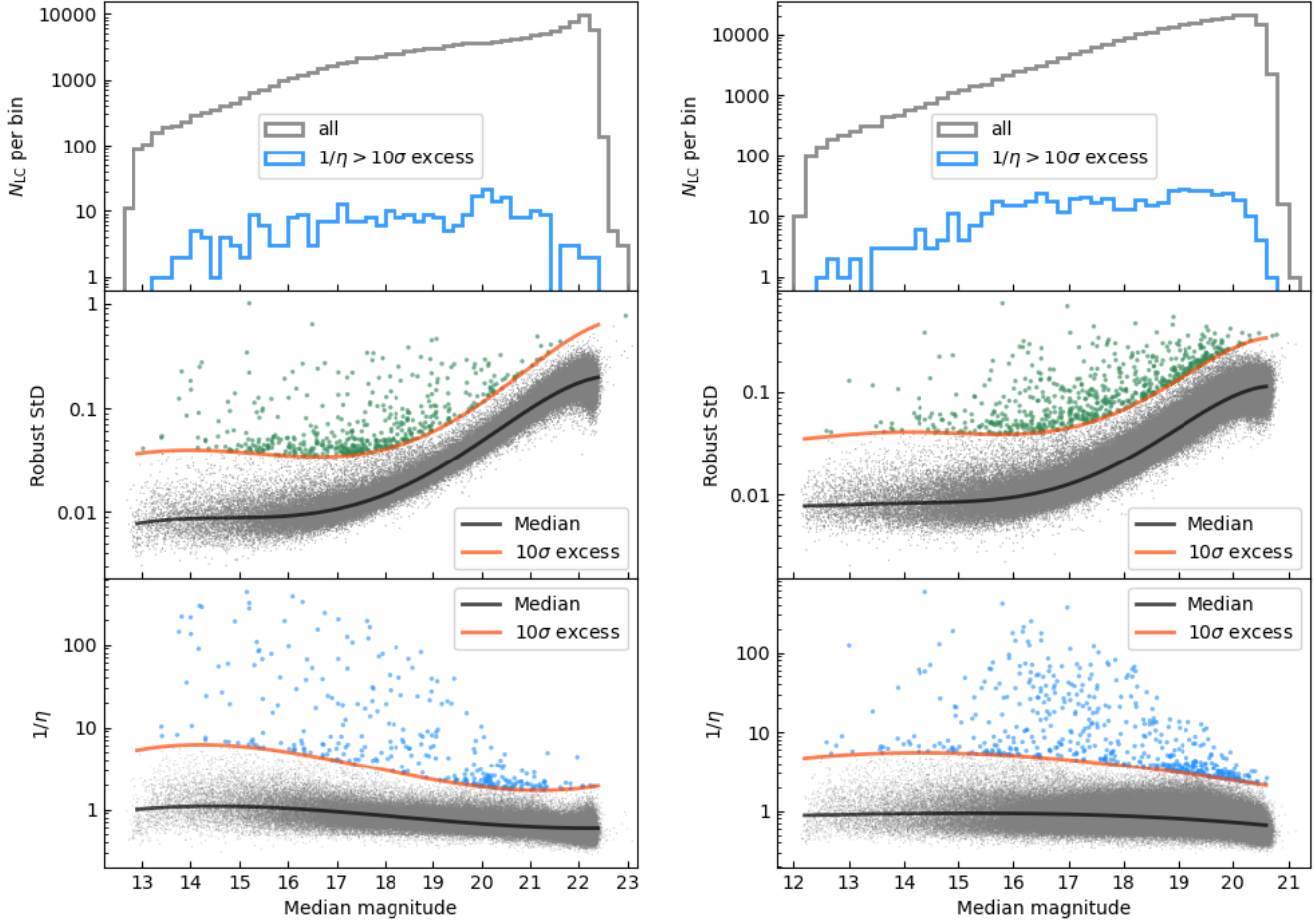


Figure 2. Distributions for number (upper), robust standard deviation (middle) and inverse von Neumann ratio (lower) against the median AB magnitude, derived from the light curves extracted from g -band observations GP-20240209 (left) and r -band observations GP-20240509 (right). *Upper panels:* The grey lines represent the number of light curves (with ≥ 20 epochs) per bin, while the blue lines represent the number of candidate variable stars (with $1/\eta$ above the 10σ threshold) per bin. The bin size is 0.2 mag. *Middle panels & Lower panels:* The black and red lines represent the medians and 10σ excesses for the distributions of variability indices, respectively. The grey and green/blue points represent the light curves with variability indices below and above the 10σ thresholds, respectively.

rate is 76% for GP-20240209 and 65% for GP-20240509, respectively. However, because robust StD is extremely insensitive to the temporary light variations in the light curves, we tended to adopt another variability index to detect the brightness variability of sources including those flaring stars.

By comparing 18 variability indices that quantify scatter and/or correlation among photometric time series, Sokolovsky et al. (2017) concluded that von Neumann ratio η (or inverse von Neumann ratio $1/\eta$, conventionally) is one of the best indices in selecting candidate variables. The von Neumann ratio can test the independence of successive brightness measurements, and is thus applied in variability detection for light curves af-

ected by outliers. The $1/\eta$ can be calculated by

$$\frac{1}{\eta} = \frac{\sum_{i=1}^N (m_i - \bar{m})^2}{\sum_{i=1}^{N-1} (m_{i+1} - m_i)^2}, \quad (1)$$

where m_i and m_{i+1} represent the i th and $(i+1)$ th magnitudes in a light curve, respectively. \bar{m} is the average magnitude over all epochs, and N denotes the number of epochs. The $1/\eta$ is expected to be 0.5 for an ideal time series following a Gaussian distribution. However, due to astrophysical variations and various photometric issues, the distributions of real photometric measurements are actually deviated from Gaussian distributions. As shown in the lower panels of Fig. 2, the $1/\eta$ decreases from ~ 1 to 0.6 along with the magnitude. Similarly, we fitted the the 10σ excesses against median

magnitudes using 3th-order polynomial models, which lead to 306 and 527 candidate variable sources selected from GP-20240209 and from GP-20240509, respectively. These candidate variable sources include a dozen of flaring stars that were missed in the selections based on robust StD. By visually checking the light curves, we found that the false positive rate drops to 60% for GP-20240209 and 53% for GP-20240509, respectively, implying that von Neumann ratio is a much better variability index to select variable stars. As both *r*- and *g*-band minute-cadence observations suggest that about 0.1% of observed sources exhibit real astrophysical variability, WFST is expected to reveal several million variable sources among five billion significantly detected sources within Galaxy in the future (Wang et al. 2023a).

Furthermore, in order to search for specific types of variable stars, we prefer to use Osten’s method and LSP to select flaring stars and periodic variable stars, respectively, while the variability indices are used as an auxiliary tool to improve the completeness of selections.

3.2. Flare detection

In order to search for fast flares in minute-/hour-timescale from minute-cadence observation data, we applied the flare selection method described in Osten et al. (2012) and the false discovery rate (FDR) analysis used by Lin et al. (2022). Before the selections, all 531,732 uninterrupted light curves (with epochs ≥ 50) were detrended using a compound model of 4th-order Fourier series and 2nd-order polynomial (see the Eq. 7 in Lin et al. 2022). Given the hour-level observations spans, the polynomial components here are intended for offsetting potential long-timescale variations induced by both astrophysical (e.g. long-period eclipsing binaries) and non-astrophysical (e.g. varied altitude angles) factors.

For obeying the normal distribution, the detrended magnitudes ($m_{\text{dtr}} = m - m_{\text{model}}$) are normalized as

$$V_i = \frac{\overline{m_{\text{dtr}}} - m_{\text{dtr},i}}{\sigma_{\text{dtr}}}, \quad (2)$$

where $m_{\text{dtr},i}$ represents *i*th detrended magnitude. $\overline{m_{\text{dtr}}}$ and σ_{dtr} represent the median and robust standard deviation of detrended magnitudes, respectively.

Following the approach introduced by Osten et al. (2012), the flares in light curves could be detected through at least two consecutive positive outliers in the time series. The index quantifying the significance of two consecutive outliers in a time series is defined as the product of continuous two normalized detrended magnitudes, namely

$$\phi_{\text{VV},i} = V_i \times V_{i+1}. \quad (3)$$

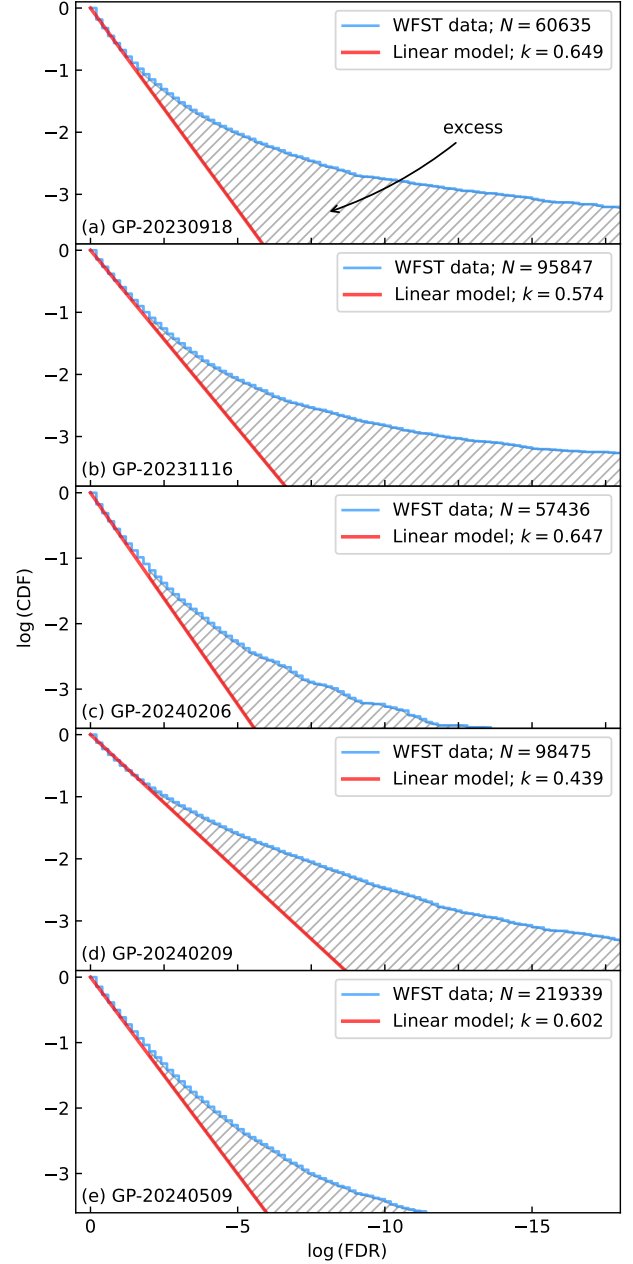


Figure 3. Cumulative distribution functions (CDFs) of false discovery rates (FDRs) for flare detection from WFST minute-cadence observations. The FDR histograms (blue solid lines) in panel a–e are given by ϕ_{VV} sequences derived from five WFST minute-cadence observations, respectively. And the red solid lines are the best-fit linear models for the histogram bins at $\log(\text{CDF}) \geq -1$. The bin size is 0.2. The shaded area indicate that the observed FDR distributions excess the models.

For the purposes of selecting flares (rather than dips or eclipses), the adopted $\phi_{\text{VV},i}$ pairs require both $V_i > 0$ and $V_{i+1} > 0$. To simplify calculations, only the maximum $\phi_{\text{VV},i}$ over a time series (i.e. $\phi_{\text{VV},\text{max}} =$

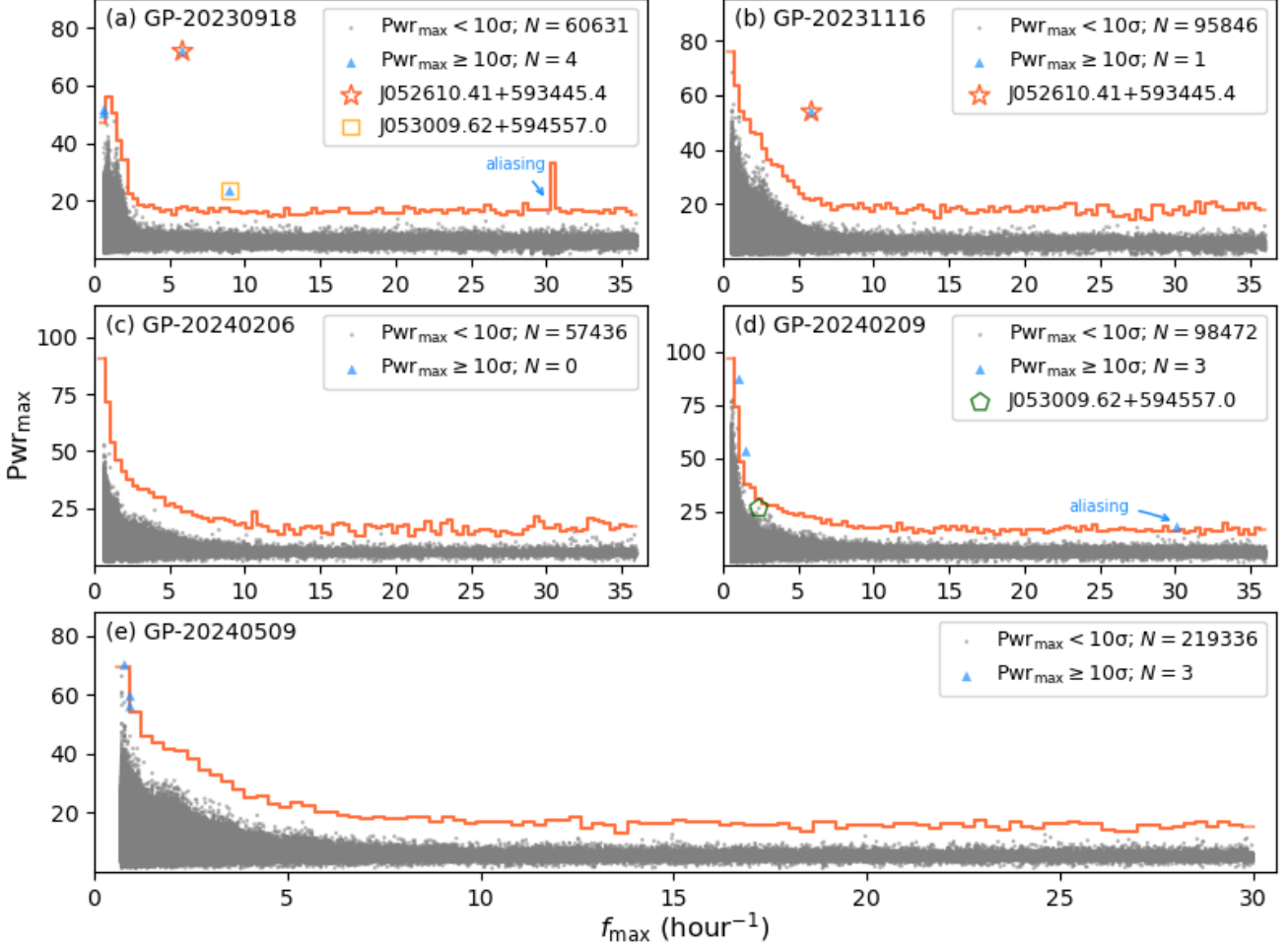


Figure 4. Distributions of maximum power Pwr_{\max} versus their corresponding frequency f_{\max} . Data points in panel a–e are given by LSPs derived from five WFST minute-cadence observations, respectively. The red solid line represents $10\text{-}\sigma$ excesses, and the total numbers (N) of sources above/below the 10σ threshold are indicated in the legends. Several interesting short-period objects are highlighted with hollow symbols.

$\max_i\{\phi_{VV,i} | v_i > 0, v_{i+1} > 0\}$) is applied to the flare detection. In other words, a light curve having a higher $\phi_{VV,\max}$ is more likely to present flares.

Benefit from the probability density function (PDF) for ϕ_{VV} given by Lin et al. (2022), we can calculate the FDRs of flares in theory for WFST light curves via

$$\text{FDR} = 1 - \left[1 - \frac{1}{2\pi} \int_{\phi_{VV,\max}}^{\infty} K_0(|x|) dx\right]^{N-1}, \quad (4)$$

where K_0 represents the special ($n = 0$) case of *modified Bessel function of the second kind* (Abramowitz & Stegun 1972), and $N - 1$ is the number of ϕ_{VV} for a time series of N epochs. The cumulative distribution functions (CDFs) of these FDRs are shown in Fig. 3. Given the prerequisite that only a small fraction of light curves exhibit flares, we fitted the the histogram bins at $\log(\text{CDF}) \geq -1$ (i.e. the cumulative distributions for 90% light curves) with a linear model,

$\log(\text{CDF}) = k \times \log(\text{FDR})$. Since the magnitudes in light curves do not tightly follow Gaussian distributions and are not completely independent of each other, it is common for the cumulative distributions of FDRs to deviate from the ideal null distribution (i.e. $\text{CDF} = \text{FDR}$, see also Lin et al. 2022). By regarding the best-fit models as the null distributions, FDRs can be calibrated via the best-fit slope k , namely $\text{FDR}_{\text{cal}} = \text{FDR}^k$. Given the non-astrophysical outliers induced by potential issues (e.g. bleeding of saturated sources) in early observation data, we adopted a tight threshold for false detection rates (i.e. $\text{FDR}_{\text{cal}} \leq 10^{-6}$), leading to 486 flaring star candidates selected from the light curves. By visually checking all candidates, we found that, 33 ones present real flares, while the most of artificial flares are arisen by the bleeding of saturated sources or the incorrect models for detrending. Nonetheless, the number of flaring stars revealed from the total 15-hour WFST ob-

servations is comparable to all flaring stars discovered among first-year TMTS observations (Lin et al. 2022; Liu et al. 2023).

However, since the observation spans are only 3–4 hours, the Osten’s method failed to model the quiescence fluxes for the “long-duration” flares lasting for $\gtrsim 1$ hour, leading to the miss of these “energetic” flares from the selections above. Given that the “energetic” flares must exhibit significantly strong variability, we visually checked the variable star candidates with high $1/\eta$ values and picked out four additional flares. These “energetic” flares having diverse light-curve morphologies are presented in following section.

3.3. Periodicity detection

Lomb–Scargle periodogram (LSP, Lomb 1976; Scargle 1982) is a common tool to reveal periodic variation signals from unevenly sampling time series. In order to reveal both short-period variable stars and general periodic variable stars, the LSPs for WFST light curves were calculated under two different sets.

3.3.1. Short-period variable stars

Aiming at searching for short-period variable stars, we calculated variance-scaled LSPs (see Eq. 1 of Coughlin et al. 2020 or Eq. 5 of Lin et al. 2022) for all uninterrupted light curves with epochs ≥ 50 within frequency from $2/T$ to f_{nyq} , where T represents the time spans of uninterrupted observations and f_{nyq} is the (pseudo-)Nyquist frequency (VanderPlas 2018). The f_{nyq} here was set to a half of average sampling rate f_0 , i.e. 1/100 Hz for 20s exposures and 1/120 Hz for 30s exposures, respectively. Due to the limitation from the lowest frequency $2/T$, these LSPs can only be used to detect variable stars with a period shorter than 1.5-2 hours.

The false alarm probability (FAP) that quantifies the significance of a periodic signal is generally inferred from the maximum power (Pwr_{max}) over a LSP (e.g. Eq. 54 of VanderPlas 2018). However, for the uninterrupted light curves obtained within single nights, the distributions of Pwr_{max} are severely affected by window functions and are thus frequency-dependent. To avoid missing short-period variable sources, Lin et al. (2023b) suggested that $\text{Pwr}_{\text{max}}-f_{\text{max}}$ diagram should be applied in the periodicity detection for single-night observations, where f_{max} is the frequency corresponding to the maximum power Pwr_{max} within a LSP. As shown in Fig. 4, f_{max} distributes over the investigated frequency ranges, while Pwr_{max} integrally tend to much higher values at the low-frequency ends. As the targeted star in both GP-20230918 and GP-20231116, the periodicity of J0526+5934 (highlighted in the panel *a, b* of Fig. 4, see

also Kosakowski et al. 2023; Lin et al. 2024; Rebassa-Mansergas et al. 2024) is well reproduced in WFST observations. Thanks to lower “noise” at higher frequency in the $\text{Pwr}_{\text{max}}-f_{\text{max}}$ diagram, a 6.7-min variable star J053009.62+594557.0 (right ascension $\alpha = 82.5401$ and declination $\delta = 59.7661$, hereafter J0530+5945, highlighted in the panel *a* of Fig. 4) emerged out of sixty thousand candidate sources.

In order to pick out periodic variable source candidates with frequency-dependent thresholds, each $\text{Pwr}_{\text{max}}-f_{\text{max}}$ diagram was divided into 100 uniform frequency intervals, and each frequency bin independently derives the thresholds corresponding to 10σ excesses. Given the thresholds, 10 (unrepeated) periodic variable source candidates were selected. By visually checking all these candidates, 9 (out of 10) ones exhibit real periodicity, while only a candidate is induced by the aliasing periodic signals around two minutes. We have tried to lower the selection threshold in order to include more candidates. However, the weak periodicity from these additional candidates is very difficult to be identified and confirmed. Nonetheless, we highlighted an interesting periodic variable star (i.e. J0530+5945) below the 10σ excesses from the observation GP-20240209 (see the panel *d* of Fig. 4). We will present further classifications for these short-period objects through the CMD in the following chapter.

3.3.2. General periodic variable stars

In order to mine and present diverse periodic variable stars from our minute-cadence observations, we spliced the uninterrupted observations having consistent pointings, i.e. GP-20230918+GP-20231116 (SO1 hereafter) and GP-20240206+GP-20240209 (SO2 hereafter). Since the observation spans are greatly extended to about 3 months/3 days for SO1/SO2, the splicing light curves are thought to be used for detecting periodic variable stars longer than tens of hours. However, due to the observation strategy developed for capturing short-period variable stars, the splicing observations actually cover minor, non-uniform phase ranges of those potential long-period variable stars. Owing to extremely uneven sampling cadence, their window functions are dramatically amplified below the frequency of about 3d^{-1} . Hence, we calculated the variance-scaled LSPs for all splicing light curves with epochs ≥ 50 within a fixed frequency range, 3d^{-1} to 12d^{-1} .

The FAPs were obtained following the independent frequency method (VanderPlas 2018), namely

$$\text{FAP} = 1 - [1 - \exp(-\text{Pwr}_{\text{max}})]^{N_{\text{eff}}}, \quad (5)$$

where N_{eff} is the effective number of independent frequencies, which is assumed to be investigated frequency

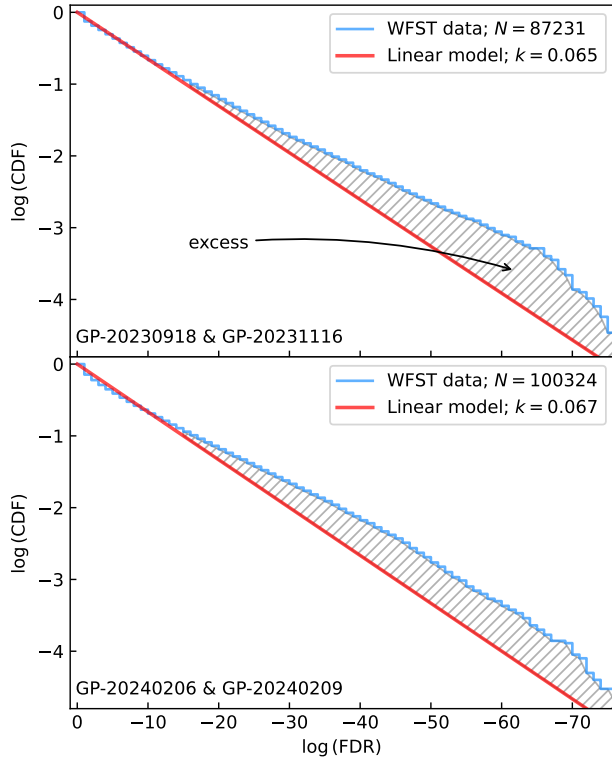


Figure 5. Cumulative distribution functions (CDFs) of false alarm probabilities (FAPs) for periodicity detection from the splicing observations. The data sets were obtained from GP-20230918+GP-20231116 (upper) and GP-20240206+GP-20240209 (lower), respectively. The blue lines represent the CDFs derived from WFST observation data, and the red lines are the best-fit linear models for the bins with $\log(\text{CDF}) \geq -1$. The bin size is 1.0 .

range in unit of expected frequency width ($\delta f = 1/T$). As Fig. 5 shows, due to the systematic overestimation of $P_{\text{wr,max}}$ induced by window functions, the cumulative distributions of FAPs are far deviated from the ideal null distribution. In order to reproduce the null distributions for the observation data, we tried to fit the the histogram bins at $\log(\text{CDF}) \geq -1$ with $\log(\text{CDF}) = k \times \log(\text{FAP})$. Similar to the approach for flare search, the FAPs were calibrated by $\text{FAP}_{\text{cal}} = \text{FAP}^k$ based on the best-fit linear models. By adopting an FAP threshold of 0.1%, 288 and 374 candidates were selected from SO1 and SO2, respectively. Among them, we visually confirmed 146 variable stars having real periodic variations. Notice that, the three-hour uninterrupted observations are not intended to serve the search of the variables in such light-variation periods. Here mining the periodic variable stars from splicing observations is in an effort to present plentiful types of variable stars in the early results of WFST.

3.4. Cross-match with Gaia DR3 catalog

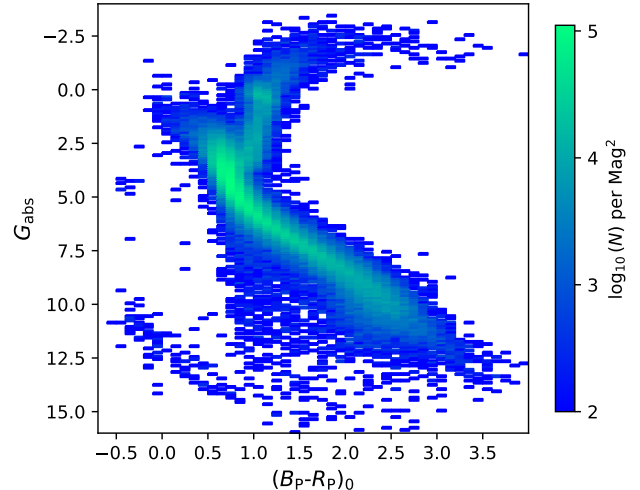


Figure 6. Density distribution of the Gaia DR3-WFST sources across the color-magnitude diagram. Only the Gaia DR3 sources having a reliable parallax measurement are included in the distribution. Both magnitudes and colors are calibrated for interstellar dust extinction and reddening. The bin size is $0.1 \times 0.1 \text{ mag}^2$.

Besides the selections based on the diverse light variations, the additional photometric and astrometric information provided from external catalogs is effective for filtering and identifying variable stars. Since CMD plays a crucial role in the classifications of short-period variable stars (Lin et al. 2023b), we cross-matched all 500,460 WFST sources (corresponding to 650,696 uninterrupted light curves having epochs ≥ 20) with Gaia DR3 sources (Gaia Collaboration et al. 2022) within 2 arcsec. As a result, 489,801 WFST sources (97.87%) match at least a Gaia counterpart. Among them, 102,509 (20.93%) Gaia sources have a reliable parallax measurement (i.e. $\varpi/\sigma_\varpi \geq 5.0$), which allow us to calculate absolute magnitudes and estimate interstellar dust extinctions.

We present the density distribution for one hundred thousand Gaia DR3-WFST sources in the CMD (Fig. 6). Both magnitudes and colors are already calibrated for interstellar dust extinction and reddening, which are obtained from three-dimensional dust map (Green et al. 2019) with the *DUSTMAPS Python* package⁵ (Green 2018). As Fig. 6 shows, the Gaia DR3-WFST sources cover diverse regions over the CMD, including main sequence, red giant branch, extreme horizontal branch and WD cooling sequence. Aiming at searching for UCBs harboring double WDs, all WFST sources were also cross-matched with the catalog of WDs in Gaia EDR3

⁵ <https://github.com/gregreen/dustmaps>

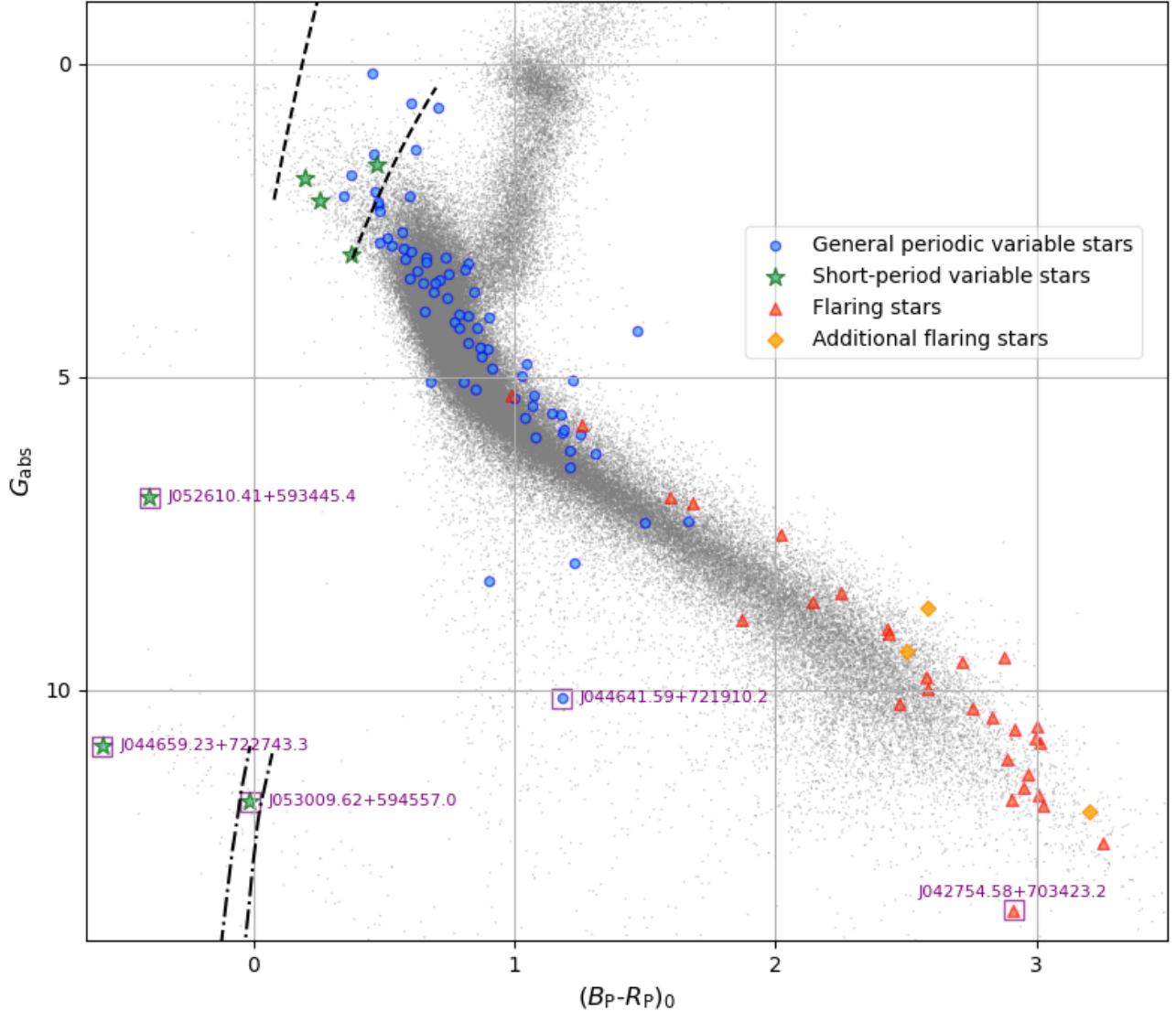


Figure 7. Distributions of periodic variable stars and flaring stars across the CMD. The general periodic variable stars, short-period variable stars and flaring stars are selected by three different methods introduced in Section 3. The additional flaring stars were discovered by visually checking the variable star candidates with high $1/\eta$ values rather than by the Osten’s method. Several interesting objects are highlighted by purple squares. The grey dots in background are the sources detected from the 15-hour WFST observations. We denote the instability strip edges of δ Scuti (Murphy et al. 2019) and ZZ Ceti (Caiazzo et al. 2021) with the dashed lines and dot-dashed lines, respectively.

(Gentile Fusillo et al. 2021), leading to 263 WD candidates identified out of the WFST sources. Benefit from the large aperture and thus high detection depth, the number of WDs covered by three pointings of WFST is comparable with the amount covered by 90 TMTS fields (Lin et al. 2022).

4. EARLY RESULTS

Following the methods introduced in previous section, we present selected periodic variable stars and flaring stars across the CMD (Fig. 7). The periodic variable stars occupy the zones of A,F,G-type main-sequence

stars while the flaring stars are concentrated on the late-type main sequence. In this section, we will show WFST performance in detecting the variable stars, and introduced several interesting objects in details.

4.1. General periodic variable stars

Among 146 selected general periodic variable stars in Section 3.3.2, 118 objects were already identified by the International Variable Star Index (VSX, Watson et al. 2006). According to the variable star types provided from VSX, 89% of them are identified as EW-type eclipsing binaries and 6% are RR Lyrae variables. Notice

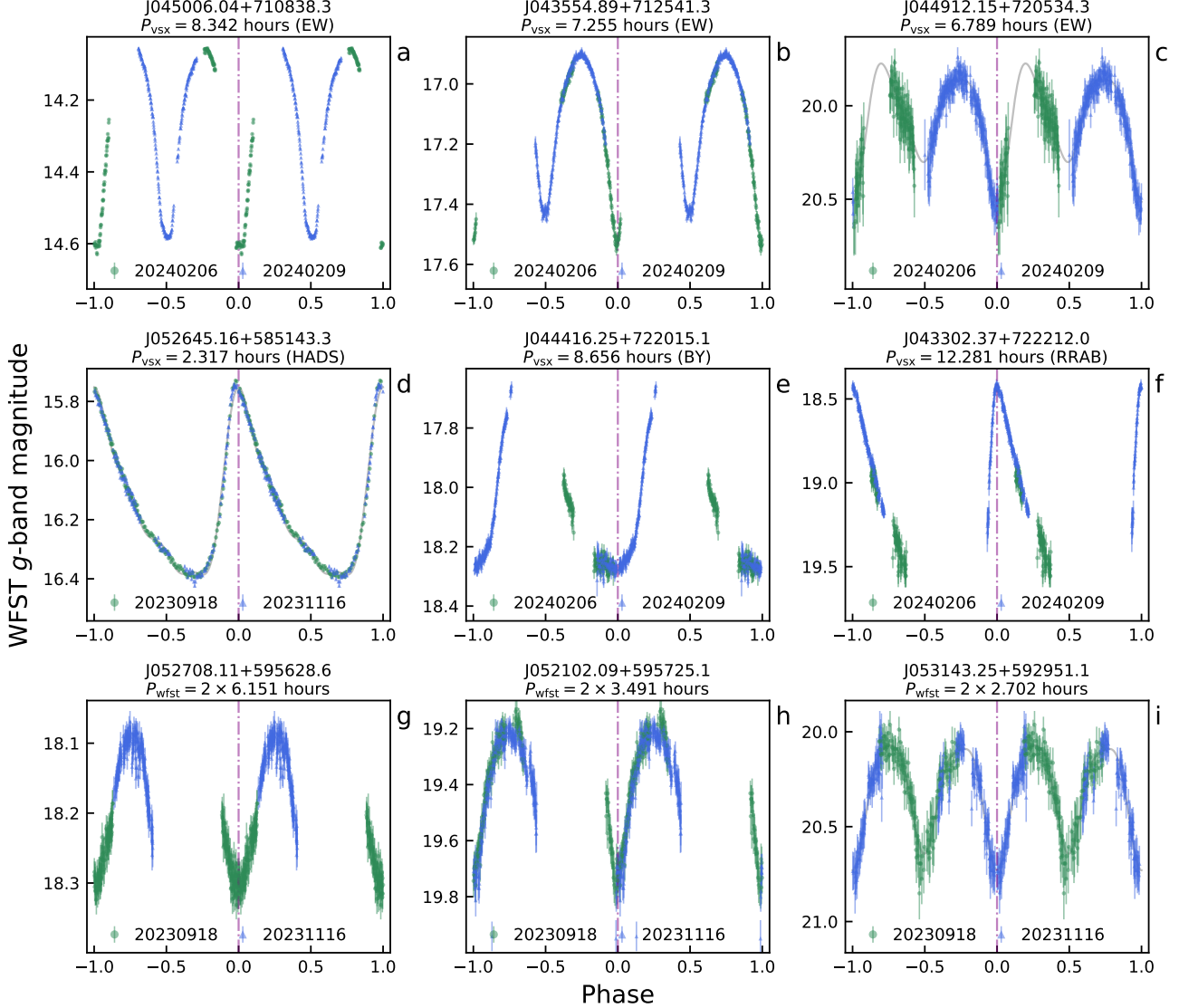


Figure 8. A gallery of phase-folded light curves for nine general periodic variable stars revealed by the splicing observations. All light curves are obtained from the g -band observations of WFST, and the exposure is 20 seconds. For the objects identified by VSX, their light curves (panel a–f) are folded by the period provided by VSX; for the variables first identified by WFST, the light curves (panel g–i) are folded using twice the photometric periods (i.e. $1/f_{\max}$) obtained from WFST LSPs. We label the classification type for the objects identified by VSX: EW = EW-type eclipsing binary, HADS = high-amplitude δ Scuti star, RRAB = RRab Lyrae, and BY = BY Draconis-type variable. The light curves having relatively complete phase coverage (i.e. panel c, d and i) are modeled using 4th-order Fourier series (the grey solid lines).

that, since the typical pulsation period of fundamental-mode (RRab) Lyrae is 0.3–1.0 day, which exceeds the investigated frequency range (i.e. 3 d^{-1} to 12 d^{-1}) of our LSPs. These pulsators were occasionally revealed when the LSPs captured their high-frequency harmonics. Fig. 8 presents phase-folded light curves for several general periodic variable stars within diverse magnitude ranges. The photometry with high signal-to-noise ratio (SNR) allows WFST independently discover eclipsing binaries and pulsating stars from 14 mag to darker than 20.5 mag. Owing to our observation strategy aiming at

searching for short-period variable stars, the phases of these “long-period” objects are incompletely covered by our observations. With the coming of regular surveys, we will systematically introduce WFST’s detection capability in periodic variable stars in the future.

A newly discovered ellipsoidal binary (candidate) containing a WD and a low-mass main-sequence (MS) star. Among the selected general periodic variable stars, a sample is found to be far deviated from the main sequence in CMD (Fig. 7), namely WFST J044641.59+721910.2 ($\alpha = 71.6733$ and

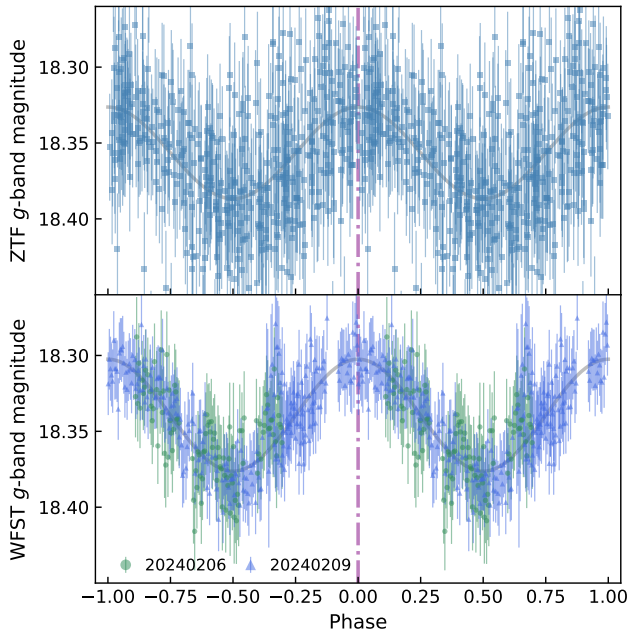


Figure 9. Phase-folded light curves of J0446+7219 provided from ZTF DR22 (upper panel) and WFST minute-cadence observations (lower panel). Both light curves are folded by the photometric period ($P = 2.95126$ hours) derived from the 6-year ZTF g -band observations. For an ellipsoidal binary, its orbital period is twice the photometric period. The grey solid lines represent the best-fit sinusoidal models.

$\delta = 72.3195$, hereafter J0446+7219). Its periodicity and sinusoidal-like light-curve profile are double checked by ZTF observations (see Fig. 9). J0446+7219 [$G_{\text{abs}} = 10.13$ mag and $(B_P - R_P)_0 = 1.18$] locates in a CMD region corresponding to magnetic CVs (Lin et al. 2023b) or WD-MS binaries (Rebassa-Mansergas et al. 2021). Due to the fact that magnetic CVs rarely exhibit sinusoidal-like light curves (see also Liu et al. 2024), we tend to support that J0446+7219 is an ellipsoidal binary with an orbital period of 5.90 hours, in which a low-mass MS is tidally deformed by its WD companion. The spectroscopic identifications on Balmer lines and TiO bands could provide further evidences to support/refuse the inference.

4.2. Short-period variable stars

As introduced in Section 3.3.1, 10 short-period variable stars were selected from the $P_{\text{wr,max}} - f_{\text{max}}$ diagrams. As the dominant “noise” sources in systematic search of interesting short-period variable stars (Lin et al. 2023b), hour-period δ Scuti stars are the main variable stars in our samples (e.g. the green stars within the classical instability strip of Fig. 7). We present an example of δ Scuti star detected by WFST in panel (a & e) of Fig. 10. With the increment in detection depths of sur-

vey telescopes, a large number of distant δ Scuti stars discovered by new instruments will be absence of credible parallax measurements from Gaia. Hence, an identification tool that can distinguish δ Scuti stars from other short-period variable stars without the CMD, needs to be developed, e.g. the distribution of δ Scuti stars in period-amplitude diagram (Lin et al. 2023b).

To test WFST’s capability in searching for and detecting short-period variable stars, 20.5-min ultracompact binary J0526+5934 (Kosakowski et al. 2023; Lin et al. 2024; Rebassa-Mansergas et al. 2024) was set as the targeted star of observation GP-20230918 and GP-20231116. As panel (b) of Fig. 10 shows, despite a long dead time (≈ 30 s) of camera, WFST can clearly reproduce the light curve for a 17.6-mag source having a variation period as short as 10.3 minutes (i.e. a half of its orbital period). An outstanding feature is that its two minimums within an orbit are distinguishable in the WFST phase-folded light curve (panel f of Fig. 10), which supports the asymmetric geometry between two ends of the tidally distorted visible component. Such a feature from J0526+5934 has not been previously revealed by ZTF (Kosakowski et al. 2023), Lijiang 2.4m Telescope (Lin et al. 2024) or 2.4m Thai National Telescope (Rebassa-Mansergas et al. 2024).

One of the darkest ZZ Ceti variables discovered yet. ZZ Ceti variables are a type of pulsating WDs with almost pure hydrogen atmospheres. Thanks to the densely sampling data from Transiting Exoplanet Survey Satellite (TESS, Ricker et al. 2015), dozens of the bright ($V < 16$) ZZ Ceti variables have been discovered (Romero et al. 2022, 2024). However, due to rapid and relatively weak light variations, only a few ZZ Ceti variables darker than 19 mag have been identified yet (Greiss et al. 2016). As introduced in Section 3.3.1, a significant 6.7-min periodic signal from J0530+5945 was revealed (see also panel c & g of Fig. 10). Given the minute-level periodic source located exactly within the instability strip of ZZ Ceti (Fig. 7), we identified this object as a new member of ZZ Ceti variables. Benefit from high detection sensitivity and accumulating (daily-cadence/minute-cadence) observational data, a large number of ZZ Ceti variables will be discovered by WFST, offsetting the absence of dark pulsating WDs in the current survey missions.

Unspecific variable hot white dwarf. J044659.23+722743.3 ($\alpha = 71.7468$ and $\delta = 72.4620$, hereafter J0446+7227) is one of the bluest stars among the stars covered by our minute-cadence observations. The color $(B_P - R_P)_0 = -0.58$ and absolute magnitude $G_{\text{abs}} = 10.89$ mag imply that J0446+7227 is a WD with an effective temperature as high as one hundred

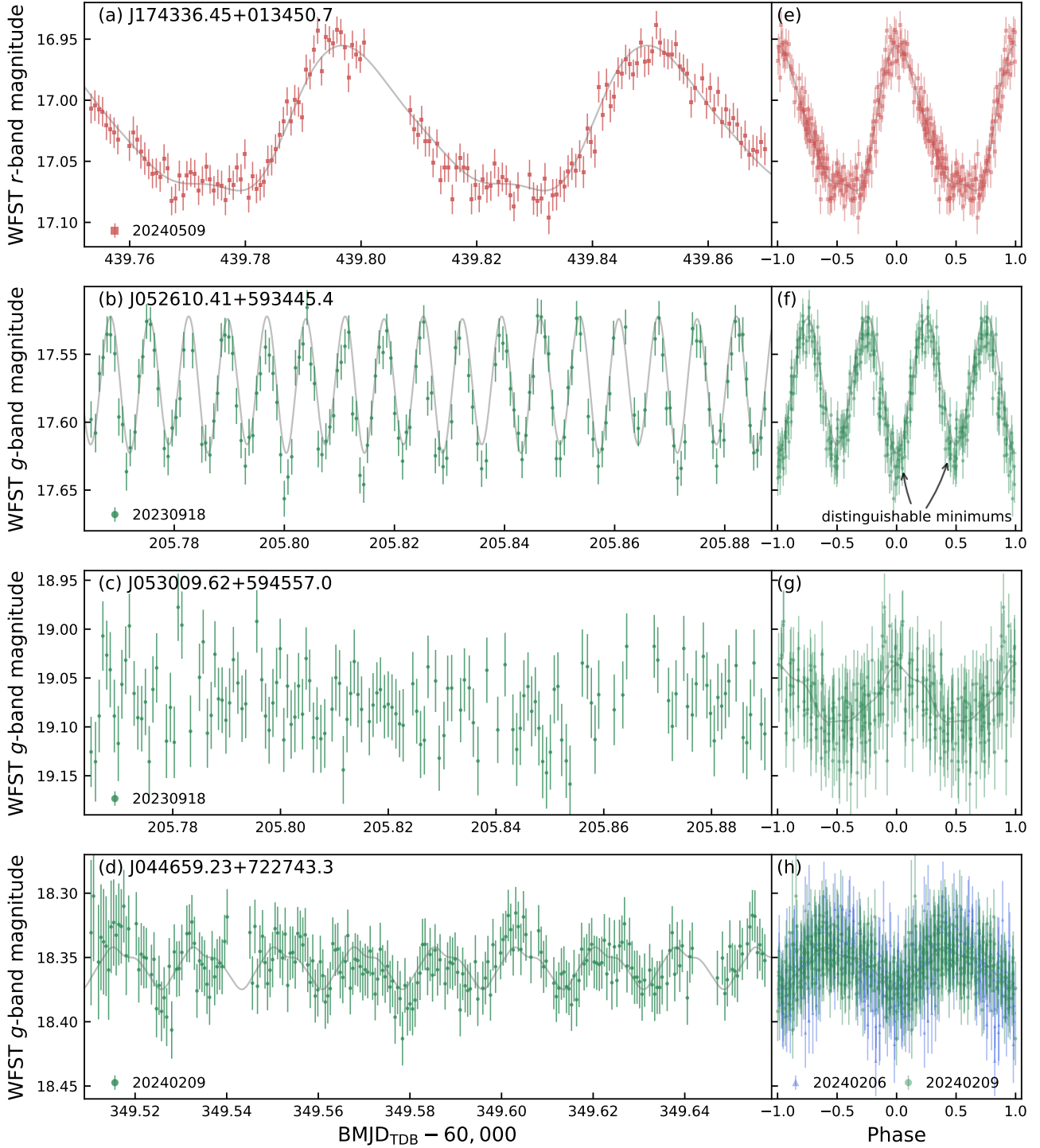


Figure 10. Uninterrupted light curves (panel a-d) and phase-folded light curves (panel e-h) for four short-period variable stars selected from WFST minute-cadence observations. These objects are 1.3-hour δ Scuti star J1743+0134 (panel a & e), 20.5-min ultracompact binary J0526+5934 (panel b & f), 6.7-min ZZ Ceti variable J0530+5945 (panel c & g), and 25.3-min unspecified variable hot WD J0530+5945 (panel d & h), respectively. To double check the periodicity, we present the phase-folded light curves for J0530+5945 obtained from two nights (panel h). The grey solid lines represent the best-fit 4th-order Fourier series.

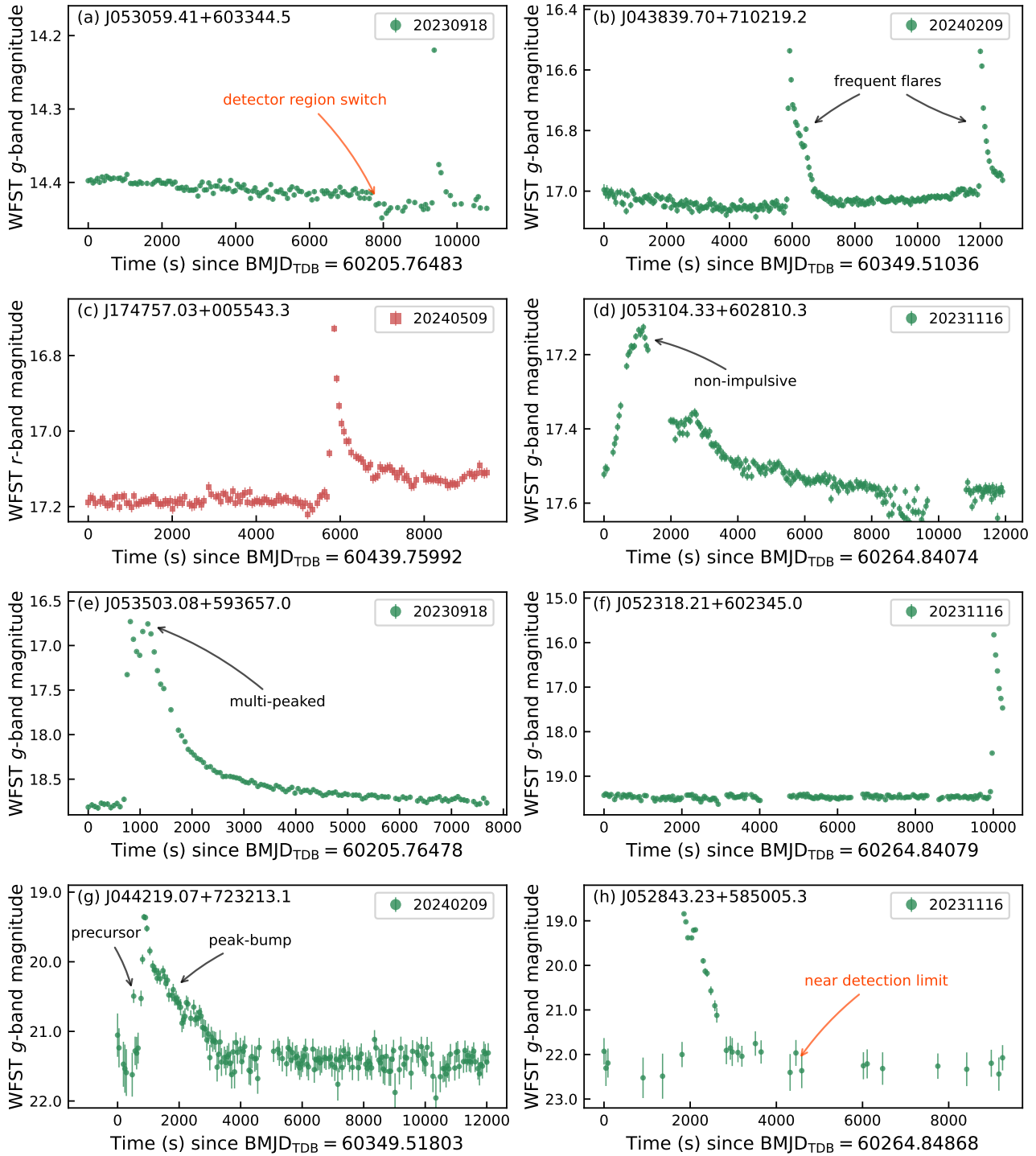


Figure 11. Uninterrupted light curves for eight flaring stars selected from WFST minute-cadence observations. All flaring stars are sorted by their quiescent magnitudes. We annotated light-curve morphology for the flares (black arrows) as well as the observation issues (red arrows). Notice that, since each (4608×4616 pixel) region on the CCDs is processed separately in current pipelines, the bright sources switching among multiple detector regions could produce tiny systematic shifts in their light curves (see panel a).

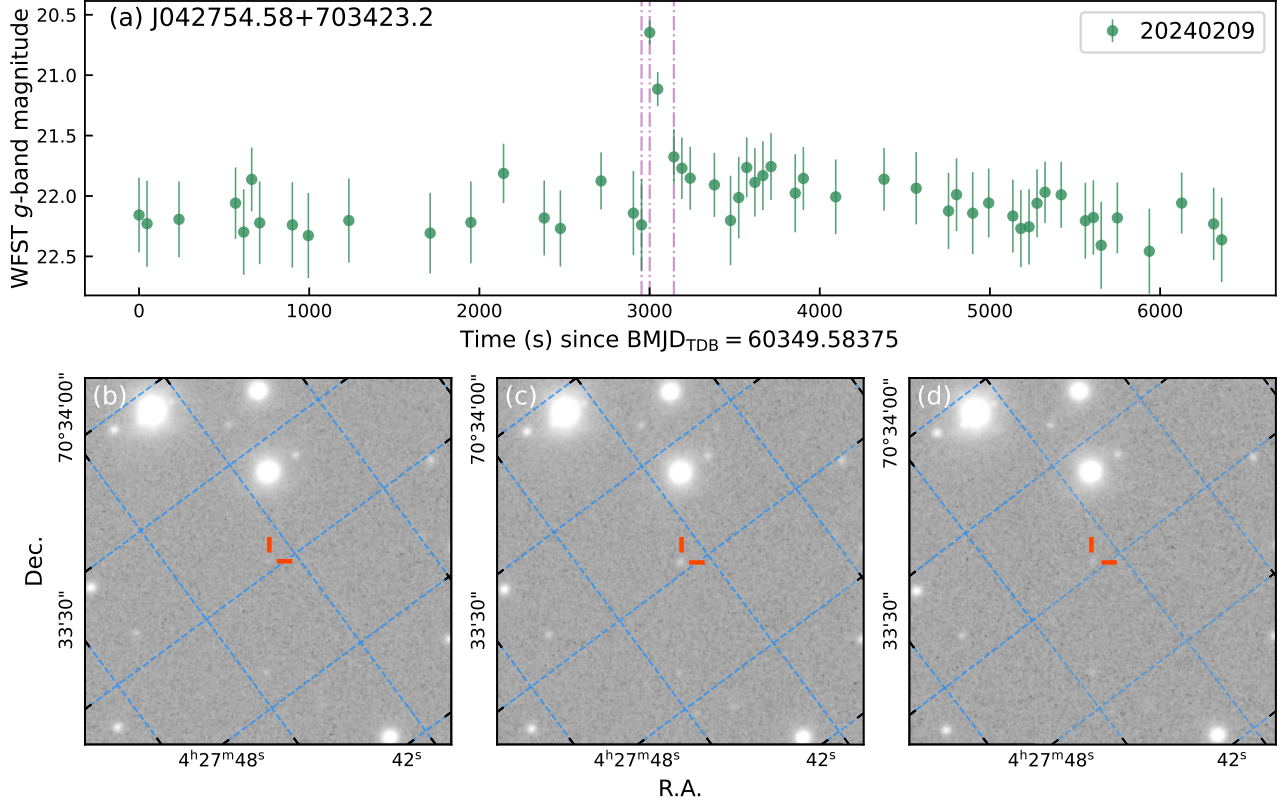


Figure 12. Uninterrupted light curve and finding charts for flaring star J0427+7034. The purple dotted-dashed lines overlapped on the light curve (panel a) indicate the epochs corresponding to the finding charts (panel b,c,d) in sequence. The red bars point the positions of J0427+7034 in the images. The size of each image is 300 pixels \times 300 pixels.

thousand Kelvin. Within the observation GP-20240209, 25.3-min periodic variations from this hot WD were marginally revealed (see Section 3.3.1). Additionally, the phase-folded light curve obtained from the observation GP-20240206 agrees the periodic variations (panel h of Fig. 10). Since its peak-to-peak amplitude is only 0.03 mag, which is comparable with WFST’s photometric uncertainties at 18.3 mag, it is challenging for other survey missions to double check the periodicity. As a hot WD with a (possible) variation period of about 25 minutes, J0446+7227 is inferred to be a candidate of variable DO WD (DOV, Córscico et al. 2019) or rapidly rotating magnetic WD (Ferrario et al. 1997; Caiazzo et al. 2021). Further spectroscopic and high-precision photometric observations could provide crucial clues to classify the object.

4.3. Flaring stars

Although dozens of time-domain survey missions are currently operating, only a few of them (e.g. TESS) are routinely performing observations in minute cadences, leading to the deficiency of stellar flares having densely observational sampling. Based on the minute-cadence observations of WFST, we present sev-

eral well sampling examples of stellar flares, ranging from 14 mag to 22 mag, in Fig. 11. In the figure, four “energetic” flares, J053104.33+602810.3 (panel d), J053503.08+593657.0 (panel e), J044219.07+723213.1 (panel g), J052843.23+585005.3 (panel h), were picked out by their high variabilities ($1/\eta$) rather than by the Osten’s method. Benefit from the densely sampling rates, these flaring stars exhibit clear light-curve profiles during flares, allowing us identify and describe temporal morphologies of flares (Davenport et al. 2014; Howard & MacGregor 2022), such as multiple peaks (panel e of Fig. 11) and a highly impulsive peak following by a “bump” (i.e. peak-bump, panel g). The minute-cadence observations also revealed a short precursor emission prior to the large flare (panel g), and a slow rising flare with a temporal structure deviated from the typical impulsive profile (panel d). Interestingly, a fast, large-amplitude flare was emitted from a very faint M dwarf J052843.23+585005.3 (panel h). Its 22-mag quiescence magnitude is challenging to be detected by current time-domain survey missions, and thus such a dramatical flaring event could be incorrectly identified as an unknown fast optical transient (FOT).

A minute-timescale flare emerged from a very dark WD binary candidate. J042754.58+703423.2 ($\alpha = 66.9774$ and $\delta = 70.5731$, hereafter J0427+7034) is a very faint object located below the red end of main sequence in the CMD (see Fig. 7). Since its color $(B_P - R_P)_0 = 2.91$ and absolute magnitude $G_{\text{abs}} = 13.51$ mag overlap on the evolutionary tracks of WD-MS binaries (Rebassa-Mansergas et al. 2021), J0427+7034 is likely a binary consisting of a very dark WD and a M dwarf companion although the potential periodic light variations generated by its orbital motion are not detected. From this object, a fast flare lasting for only a few minutes was occasionally captured by WFST (see panel a of Fig. 12). In order to confirm the abrupt light variation, we visually checked its images exposed before, on and after the flaring event: the source was almost invisible before the event (panel b), then it significantly became bright within a minute (panel c) and decayed gradually (panel d). Such a transient flaring event from a 22-mag source is almost impossible to be captured by other survey instruments. In the binary system of WD+M dwarf, the optical flares are likely induced by chromospheric activity of M dwarf or by accretion along the magnetic field lines of WD (Pelisoli et al. 2023).

5. SUMMARY

During the commissioning and pilot observation phases, we executed WFST minute-cadence observations on three different fields of Galactic plane, with a total on-source time of about 13 hours. The accumulated fractions for the position deviations suggest that WFST’s astrometric precision is better than 0.16 arcsec for 90% astrometric measurements in these observations. By cross-matching all photometric measurements within a radius of 1 arcsec, 650,696 uninterrupted light curves having at least 20 epochs, corresponding to 500,460 un-repeated WFST sources, were extracted from our observation data.

Via screening variable sources with variability index of $1/\eta$ and visually checking selected light curves, we found that about 0.1% of observed sources exhibit real astrophysical variability. In order to select light curves covering fast flaring events, 486 flaring star candidates were selected from the uninterrupted light curves (with epochs ≥ 50) through the Osten’s method, but only 33 ones show real flares by visually checking. Additionally, 4 flaring stars exhibiting “energetic” flaring events were discovered from the variable star candidates with significantly high $1/\eta$ values. By calculating the Lomb–Scargle periodograms for the uninterrupted light curves (with

epochs ≥ 50) and plotting the $P_{\text{wr,max}} - f_{\text{max}}$ diagrams, 10 short-period variable stars (with periods from several minutes to tens of minutes) were picked out. Additionally, 146 general periodic variable stars (with periods longer than 2 hours) were selected from splicing observations GP-20230918+GP-20231116 and GP-20240206+GP-20240209.

By cross-matching 500,460 WFST sources with Gaia DR3 catalog, we found that 97.87% of them have at least a Gaia counterpart, and 20.93% of these Gaia sources have a reliable parallax measurement, which support determining their positions in the CMD. Referring to the catalog of WDs from Gaia EDR3 (Gentile Fusillo et al. 2021), there are at least 263 WD candidates covered by the WFST observations.

We presented the WFST light curves for a few periodic variable stars and flaring stars picked from our minute-cadence observations, and tried to identify the selected variable sources via their positions in the CMD (Fig. 7). Besides the dominant EW-type eclipsing binaries and pulsating stars (e.g. RR Lyrae variables) among the selected general periodic variable stars, a 5.9-hr ellipsoidal binary candidate consist of a WD and a low-mass MS was first discovered from our observation data. The selected short-period variable stars include a few δ Scuti stars, a known ultracompact binary (the targeted star of this field), a newly discovered and very faint ZZ Ceti variable, and an unspecific variable hot white dwarf. Furthermore, our minute-cadence observations captured flaring stars from 14 mag to 22.5 mag, covering diverse flare temporal structures, such as multi-peaked and peak-bump flares. We also highlighted a minute-timescale flare emerged from a candidate WD binary, while it is challenging for current survey missions to capture such a fast flare from a 22-mag star.

In conclusion, benefit from large aperture and thus deep detection limit, WFST can efficiently detect and reveal short-period variable stars and fast flaring stars in unexplored parameter spaces, thus leading to new opportunities in discovering unique variable sources in the northern sky.

The Wide Field Survey Telescope (WFST) is a joint facility of the University of Science and Technology of China, Purple Mountain Observatory. J. L. is supported by the National Natural Science Foundation of China (NSFC; Grant Numbers 12403038), the Fundamental Research Funds for the Central Universities (Grant Numbers WK2030000089), and the Cyrus Chun Ying Tang Foundations.

REFERENCES

- Abramowitz, M., & Stegun, I. A. 1972, *Handbook of Mathematical Functions* (New York: Dover)
- Aizawa, M., Kawana, K., Kashiyama, K., et al. 2022, *PASJ*, 74, 1069, doi: [10.1093/pasj/psac056](https://doi.org/10.1093/pasj/psac056)
- Amaro-Seoane, P., Audley, H., Babak, S., et al. 2017, arXiv e-prints, arXiv:1702.00786, doi: [10.48550/arXiv.1702.00786](https://doi.org/10.48550/arXiv.1702.00786)
- Argiroffi, C., Reale, F., Drake, J. J., et al. 2019, *Nature Astronomy*, 3, 742, doi: [10.1038/s41550-019-0781-4](https://doi.org/10.1038/s41550-019-0781-4)
- Bellm, E. C., Kulkarni, S. R., Graham, M. J., et al. 2019, *PASP*, 131, 018002, doi: [10.1088/1538-3873/aaecbe](https://doi.org/10.1088/1538-3873/aaecbe)
- Borowicz, J., Pietrukowicz, P., Skowron, J., et al. 2023a, *AcA*, 73, 265, doi: [10.32023/0001-5237/73.4.2](https://doi.org/10.32023/0001-5237/73.4.2)
- Borowicz, J., Pietrukowicz, P., Mróz, P., et al. 2023b, *AcA*, 73, 1, doi: [10.32023/0001-5237/73.1.1](https://doi.org/10.32023/0001-5237/73.1.1)
- Burdge, K. B., Coughlin, M. W., Fuller, J., et al. 2019, *Nature*, 571, 528, doi: [10.1038/s41586-019-1403-0](https://doi.org/10.1038/s41586-019-1403-0)
- Burdge, K. B., Prince, T. A., Fuller, J., et al. 2020, *ApJ*, 905, 32, doi: [10.3847/1538-4357/abc261](https://doi.org/10.3847/1538-4357/abc261)
- Burdge, K. B., El-Badry, K., Marsh, T. R., et al. 2022a, *Nature*, 610, 467, doi: [10.1038/s41586-022-05195-x](https://doi.org/10.1038/s41586-022-05195-x)
- Burdge, K. B., Marsh, T. R., Fuller, J., et al. 2022b, *Nature*, 605, 41, doi: [10.1038/s41586-022-04551-1](https://doi.org/10.1038/s41586-022-04551-1)
- Byrne, C. M., & Jeffery, C. S. 2018, *MNRAS*, 481, 3810, doi: [10.1093/mnras/sty2545](https://doi.org/10.1093/mnras/sty2545)
- . 2020, *MNRAS*, 492, 232, doi: [10.1093/mnras/stz3486](https://doi.org/10.1093/mnras/stz3486)
- Byrne, C. M., Stanway, E. R., & Eldridge, J. J. 2021, *MNRAS*, 507, 621, doi: [10.1093/mnras/stab2115](https://doi.org/10.1093/mnras/stab2115)
- Caiazzo, I., Burdge, K. B., Fuller, J., et al. 2021, *Nature*, 595, 39, doi: [10.1038/s41586-021-03615-y](https://doi.org/10.1038/s41586-021-03615-y)
- Chambers, K. C., Magnier, E. A., Metcalfe, N., et al. 2016, arXiv e-prints, arXiv:1612.05560, doi: [10.48550/arXiv.1612.05560](https://doi.org/10.48550/arXiv.1612.05560)
- Chang, S.-W., Wolf, C., Onken, C. A., & Bessell, M. S. 2024, *MNRAS*, 529, 1414, doi: [10.1093/mnras/stae637](https://doi.org/10.1093/mnras/stae637)
- Córsico, A. H., Althaus, L. G., Miller Bertolami, M. M., & Kepler, S. O. 2019, *A&A Rv*, 27, 7, doi: [10.1007/s00159-019-0118-4](https://doi.org/10.1007/s00159-019-0118-4)
- Coughlin, M. W., Burdge, K., Duev, D. A., et al. 2020, arXiv e-prints, arXiv:2009.14071, <https://arxiv.org/abs/2009.14071>
- Davenport, J. R. A., Hawley, S. L., Hebb, L., et al. 2014, *ApJ*, 797, 122, doi: [10.1088/0004-637X/797/2/122](https://doi.org/10.1088/0004-637X/797/2/122)
- Feng, F. B., Rui, Y. C., Du, Z. M., et al. 2024a, *Acta Astronomica Sinica*, 65, 34, doi: [10.15940/j.cnki.0001-5245.2024.04.001](https://doi.org/10.15940/j.cnki.0001-5245.2024.04.001)
- Feng, Q., Wang, H., Zhang, H.-f., et al. 2024b, in *Society of Photo-Optical Instrumentation Engineers (SPIE) Conference Series*, Vol. 13096, Ground-based and Airborne Instrumentation for Astronomy X, ed. J. J. Bryant, K. Motohara, & J. R. D. Vernet, 130963V, doi: [10.1117/12.3018237](https://doi.org/10.1117/12.3018237)
- Ferrario, L., Vennes, S., Wickramasinghe, D. T., Bailey, J. A., & Christian, D. J. 1997, *MNRAS*, 292, 205, doi: [10.1093/mnras/292.2.205](https://doi.org/10.1093/mnras/292.2.205)
- Finch, E., Bartolucci, G., Chucherko, D., et al. 2022, arXiv e-prints, arXiv:2210.10812, doi: [10.48550/arXiv.2210.10812](https://doi.org/10.48550/arXiv.2210.10812)
- Flewelling, H. A., Magnier, E. A., Chambers, K. C., et al. 2020, *ApJS*, 251, 7, doi: [10.3847/1538-4365/abb82d](https://doi.org/10.3847/1538-4365/abb82d)
- Gaia Collaboration, Prusti, T., de Bruijne, J. H. J., et al. 2016, *A&A*, 595, A1, doi: [10.1051/0004-6361/201629272](https://doi.org/10.1051/0004-6361/201629272)
- Gaia Collaboration, Vallenari, A., Brown, A. G. A., et al. 2022, arXiv e-prints, arXiv:2208.00211, doi: [10.48550/arXiv.2208.00211](https://doi.org/10.48550/arXiv.2208.00211)
- Geng, Z., Wang, Z.-y., Zheng, Z.-h., et al. 2024, in *Society of Photo-Optical Instrumentation Engineers (SPIE) Conference Series*, Vol. 13101, Software and Cyberinfrastructure for Astronomy VIII, ed. J. Ibsen & G. Chiozzi, 131010K, doi: [10.1117/12.3016395](https://doi.org/10.1117/12.3016395)
- Gentile Fusillo, N. P., Tremblay, P. E., Cukanovaite, E., et al. 2021, *MNRAS*, 508, 3877, doi: [10.1093/mnras/stab2672](https://doi.org/10.1093/mnras/stab2672)
- Green, G. M. 2018, *The Journal of Open Source Software*, 3, 695, doi: [10.21105/joss.00695](https://doi.org/10.21105/joss.00695)
- Green, G. M., Schlafly, E., Zucker, C., Speagle, J. S., & Finkbeiner, D. 2019, *ApJ*, 887, 93, doi: [10.3847/1538-4357/ab5362](https://doi.org/10.3847/1538-4357/ab5362)
- Greiss, S., Hermes, J. J., Gänsicke, B. T., et al. 2016, *MNRAS*, 457, 2855, doi: [10.1093/mnras/stw053](https://doi.org/10.1093/mnras/stw053)
- Güdel, M., Audard, M., Skinner, S. L., & Horvath, M. I. 2002, *ApJL*, 580, L73, doi: [10.1086/345404](https://doi.org/10.1086/345404)
- Günther, M. N., Zhan, Z., Seager, S., et al. 2020, *AJ*, 159, 60, doi: [10.3847/1538-3881/ab5d3a](https://doi.org/10.3847/1538-3881/ab5d3a)
- Guo, F., Lin, J., Wang, X., et al. 2024, *MNRAS*, 528, 6997, doi: [10.1093/mnras/stae404](https://doi.org/10.1093/mnras/stae404)
- Hils, D., Bender, P. L., & Webbink, R. F. 1990, *ApJ*, 360, 75, doi: [10.1086/169098](https://doi.org/10.1086/169098)
- Howard, W. S., & MacGregor, M. A. 2022, *ApJ*, 926, 204, doi: [10.3847/1538-4357/ac426e](https://doi.org/10.3847/1538-4357/ac426e)
- Huang, S.-J., Hu, Y.-M., Korol, V., et al. 2020, *PhRvD*, 102, 063021, doi: [10.1103/PhysRevD.102.063021](https://doi.org/10.1103/PhysRevD.102.063021)

- Jurić, M., Kantor, J., Lim, K. T., et al. 2017, in *Astronomical Society of the Pacific Conference Series*, Vol. 512, *Astronomical Data Analysis Software and Systems XXV*, ed. N. P. F. Lorente, K. Shortridge, & R. Wayth, 279
- Kosakowski, A., Kupfer, T., Bergeron, P., & Littenberg, T. B. 2023, *ApJ*, 959, 114, doi: [10.3847/1538-4357/ad0ce9](https://doi.org/10.3847/1538-4357/ad0ce9)
- Kupfer, T., Bauer, E. B., Burdge, K. B., et al. 2019, *ApJL*, 878, L35, doi: [10.3847/2041-8213/ab263c](https://doi.org/10.3847/2041-8213/ab263c)
- Kupfer, T., Prince, T. A., van Roestel, J., et al. 2021, *MNRAS*, 505, 1254, doi: [10.1093/mnras/stab1344](https://doi.org/10.1093/mnras/stab1344)
- Lei, L., Zhu, Q.-F., Kong, X., et al. 2023, *Research in Astronomy and Astrophysics*, 23, 035013, doi: [10.1088/1674-4527/acb877](https://doi.org/10.1088/1674-4527/acb877)
- Lin, J., & Yu, W. 2018, *MNRAS*, 474, 1922, doi: [10.1093/mnras/stx2818](https://doi.org/10.1093/mnras/stx2818)
- Lin, J., Wang, X., Mo, J., et al. 2022, *MNRAS*, 509, 2362, doi: [10.1093/mnras/stab2812](https://doi.org/10.1093/mnras/stab2812)
- Lin, J., Wu, C., Wang, X., et al. 2023a, *Nature Astronomy*, 7, 223, doi: [10.1038/s41550-022-01783-z](https://doi.org/10.1038/s41550-022-01783-z)
- Lin, J., Wang, X., Mo, J., et al. 2023b, *MNRAS*, 523, 2172, doi: [10.1093/mnras/stad994](https://doi.org/10.1093/mnras/stad994)
- Lin, J., Wu, C., Xiong, H., et al. 2024, *Nature Astronomy*, 8, 491, doi: [10.1038/s41550-023-02188-2](https://doi.org/10.1038/s41550-023-02188-2)
- Liu, Q., Lin, J., Wang, X., et al. 2023, *MNRAS*, 523, 2193, doi: [10.1093/mnras/stad365](https://doi.org/10.1093/mnras/stad365)
- . 2024, *Universe*, 10, 337, doi: [10.3390/universe10090337](https://doi.org/10.3390/universe10090337)
- Lomb, N. R. 1976, *Ap&SS*, 39, 447, doi: [10.1007/BF00648343](https://doi.org/10.1007/BF00648343)
- Lou, Z., Liang, M., Yao, D., et al. 2016, in *Society of Photo-Optical Instrumentation Engineers (SPIE) Conference Series*, Vol. 10154, *Society of Photo-Optical Instrumentation Engineers (SPIE) Conference Series*, 101542A, doi: [10.1117/12.2248371](https://doi.org/10.1117/12.2248371)
- Macfarlane, S. A., Toma, R., Ramsay, G., et al. 2015, *MNRAS*, 454, 507, doi: [10.1093/mnras/stv1989](https://doi.org/10.1093/mnras/stv1989)
- Magnier, E. A., Schlafly, E. F., Finkbeiner, D. P., et al. 2020, *ApJS*, 251, 6, doi: [10.3847/1538-4365/abb82a](https://doi.org/10.3847/1538-4365/abb82a)
- Masci, F. J., Laher, R. R., Rusholme, B., et al. 2019, *PASP*, 131, 018003, doi: [10.1088/1538-3873/aae8ac](https://doi.org/10.1088/1538-3873/aae8ac)
- McWhirter, P. R., & Lam, M. C. 2022, *MNRAS*, 511, 4971, doi: [10.1093/mnras/stac291](https://doi.org/10.1093/mnras/stac291)
- Meng, X.-C., Han, Z.-W., Podsiadlowski, P., & Li, J. 2020, *ApJ*, 903, 100, doi: [10.3847/1538-4357/abbb8e](https://doi.org/10.3847/1538-4357/abbb8e)
- Murphy, S. J., Hey, D., Van Reeth, T., & Bedding, T. R. 2019, *MNRAS*, 485, 2380, doi: [10.1093/mnras/stz590](https://doi.org/10.1093/mnras/stz590)
- Murphy, T., Chatterjee, S., Kaplan, D. L., et al. 2013, *PASA*, 30, e006, doi: [10.1017/pasa.2012.006](https://doi.org/10.1017/pasa.2012.006)
- Murphy, T., Kaplan, D. L., Stewart, A. J., et al. 2021, *PASA*, 38, e054, doi: [10.1017/pasa.2021.44](https://doi.org/10.1017/pasa.2021.44)
- Ofek, E. O., Soumagnac, M., Nir, G., et al. 2020, *MNRAS*, 499, 5782, doi: [10.1093/mnras/staa2814](https://doi.org/10.1093/mnras/staa2814)
- Osten, R. A., Kowalski, A., Sahu, K., & Hawley, S. L. 2012, *ApJ*, 754, 4, doi: [10.1088/0004-637X/754/1/4](https://doi.org/10.1088/0004-637X/754/1/4)
- Pelisoli, I., Marsh, T. R., Buckley, D. A. H., et al. 2023, *Nature Astronomy*, 7, 931, doi: [10.1038/s41550-023-01995-x](https://doi.org/10.1038/s41550-023-01995-x)
- Pietrukowicz, P., Dziembowski, W. A., Latour, M., et al. 2017, *Nature Astronomy*, 1, 0166, doi: [10.1038/s41550-017-0166](https://doi.org/10.1038/s41550-017-0166)
- Pigulski, A., Kotysz, K., & Kołaczek-Szymański, P. A. 2022, *A&A*, 663, A62, doi: [10.1051/0004-6361/202243293](https://doi.org/10.1051/0004-6361/202243293)
- Rappaport, S., Joss, P. C., & Webbink, R. F. 1982, *ApJ*, 254, 616, doi: [10.1086/159772](https://doi.org/10.1086/159772)
- Rebassa-Mansergas, A., Solano, E., Jiménez-Esteban, F. M., et al. 2021, *MNRAS*, 506, 5201, doi: [10.1093/mnras/stab2039](https://doi.org/10.1093/mnras/stab2039)
- Rebassa-Mansergas, A., Hollands, M., Parsons, S. G., et al. 2024, *A&A*, 686, A221, doi: [10.1051/0004-6361/202449519](https://doi.org/10.1051/0004-6361/202449519)
- Reid, H. A. S., Vilmer, N., & Kontar, E. P. 2014, *A&A*, 567, A85, doi: [10.1051/0004-6361/201321973](https://doi.org/10.1051/0004-6361/201321973)
- Ren, L., Li, C., Ma, B., et al. 2023, *ApJS*, 264, 39, doi: [10.3847/1538-4365/aca09e](https://doi.org/10.3847/1538-4365/aca09e)
- Ricker, G. R., Winn, J. N., Vanderspek, R., et al. 2015, *Journal of Astronomical Telescopes, Instruments, and Systems*, 1, 014003, doi: [10.1117/1.JATIS.1.1.014003](https://doi.org/10.1117/1.JATIS.1.1.014003)
- Romero, A. D., Kepler, S. O., Oliveira da Rosa, G., & Hermes, J. J. 2024, *arXiv e-prints*, arXiv:2407.07260, doi: [10.48550/arXiv.2407.07260](https://doi.org/10.48550/arXiv.2407.07260)
- Romero, A. D., Kepler, S. O., Hermes, J. J., et al. 2022, *MNRAS*, 511, 1574, doi: [10.1093/mnras/stac093](https://doi.org/10.1093/mnras/stac093)
- Ruiter, A. J., Belczynski, K., Benacquista, M., Larson, S. L., & Williams, G. 2010, *ApJ*, 717, 1006, doi: [10.1088/0004-637X/717/2/1006](https://doi.org/10.1088/0004-637X/717/2/1006)
- Scargle, J. D. 1982, *ApJ*, 263, 835, doi: [10.1086/160554](https://doi.org/10.1086/160554)
- Sokolovsky, K. V., Gavras, P., Karamelas, A., et al. 2017, *MNRAS*, 464, 274, doi: [10.1093/mnras/stw2262](https://doi.org/10.1093/mnras/stw2262)
- Toma, R., Ramsay, G., Macfarlane, S., et al. 2016, *MNRAS*, 463, 1099, doi: [10.1093/mnras/stw2079](https://doi.org/10.1093/mnras/stw2079)
- VanderPlas, J. T. 2018, *ApJS*, 236, 16, doi: [10.3847/1538-4365/aab766](https://doi.org/10.3847/1538-4365/aab766)
- Wang, B., Chen, W.-C., Liu, D.-D., et al. 2021, *MNRAS*, 506, 4654, doi: [10.1093/mnras/stab2032](https://doi.org/10.1093/mnras/stab2032)
- Wang, T., Liu, G., Cai, Z., et al. 2023a, *Science China Physics, Mechanics, and Astronomy*, 66, 109512, doi: [10.1007/s11433-023-2197-5](https://doi.org/10.1007/s11433-023-2197-5)

- Wang, Y., Murphy, T., Lenc, E., et al. 2023b, MNRAS, 523, 5661, doi: [10.1093/mnras/stad1727](https://doi.org/10.1093/mnras/stad1727)
- Watson, C. L., Henden, A. A., & Price, A. 2006, Society for Astronomical Sciences Annual Symposium, 25, 47
- Williams, K. A., Hermes, J. J., & Vanderbosch, Z. P. 2022, AJ, 164, 131, doi: [10.3847/1538-3881/ac8543](https://doi.org/10.3847/1538-3881/ac8543)
- Wu, T., & Li, Y. 2018, MNRAS, 478, 3871, doi: [10.1093/mnras/sty1347](https://doi.org/10.1093/mnras/sty1347)
- Xiong, H., Casagrande, L., Chen, X., et al. 2022, A&A, 668, A112, doi: [10.1051/0004-6361/202244571](https://doi.org/10.1051/0004-6361/202244571)
- Yang, H., Liu, J., Qiao, E., et al. 2018, ApJ, 859, 87, doi: [10.3847/1538-4357/aabd31](https://doi.org/10.3847/1538-4357/aabd31)
- Zhang, H.-f., Feng, Q., Wang, J., et al. 2024, in Society of Photo-Optical Instrumentation Engineers (SPIE) Conference Series, Vol. 13103, X-Ray, Optical, and Infrared Detectors for Astronomy XI, ed. A. D. Holland & K. Minoglou, 131030V, doi: [10.1117/12.3012637](https://doi.org/10.1117/12.3012637)
- Zhang, J.-C., Wang, X.-F., Mo, J., et al. 2020, PASP, 132, 125001, doi: [10.1088/1538-3873/abbea2](https://doi.org/10.1088/1538-3873/abbea2)
- Zhu, Z.-y., Cao, Z.-h., Sun, Y.-c., et al. 2024, in Society of Photo-Optical Instrumentation Engineers (SPIE) Conference Series, Vol. 13098, Observatory Operations: Strategies, Processes, and Systems X, ed. C. R. Benn, A. Chrysostomou, & L. J. Storrie-Lombardi, 1309810, doi: [10.1117/12.3017283](https://doi.org/10.1117/12.3017283)